

Interface propagation in fiber bundles: Local, mean-field and intermediate range-dependent statistics

Soumyajyoti Biswas and Lucas Goehring

Max Planck Institute for Dynamics and Self-Organization, Am Fassberg 17,
Göttingen-37077, Germany.

E-mail: soumyajyoti.biswas@ds.mpg.de, lucas.goehring@ds.mpg.de

Abstract. The fiber bundle model in two-dimensions is essentially an array of elements in square lattice that break when sufficient load is applied on them. With a local loading mechanism, this gives an interface between the broken and unbroken parts of the model. The interface can propagate through the system depending on the loading rate and disorder present in the failure thresholds of the fibers. In the presence of a quasi-static drive, the intermittent dynamics of the interface mimic front propagation in disordered media. Such situations appear in diverse physical systems such as mode-I crack propagation, domain wall dynamics in magnets, charge density waves, contact line in wetting etc. We study the effect of the range of interaction, i.e. neighborhood of the interface affected following a local perturbation, on the statistics of the intermittent dynamics of the front. There exists a crossover from local to global behavior as the range of interaction grows and a continuously varying ‘universality’ in the intermediate range. This means that the range is a relevant parameter of any resulting physics. This is particularly relevant in view of the fact that there is a scatter in the experimental observations of the exponents, in even idealized experiments on fracture fronts, and also a possibility in changing the interaction range in real samples.

1. Introduction

The fiber bundle model, introduced in Ref. [1], is a useful approach for modeling catastrophic failures in disordered solids from a microscopic point of view [2, 3]. It aims at using the minimal ingredients that nonetheless capture the universal statistical features associated with phenomena [4, 5, 6] such as: the breaking of disordered samples like wood [7], glass [8], polymeric foam [9], and paper [10]; roughness of fracture fronts in peeling experiments with PDMS samples [11, 12, 13]; and precursor events in the catastrophic collapse of cliffs [14], landslides [15] etc. In particular, it considers a set of elements having finite failure thresholds drawn from a probability distribution as a simple model for a disordered solid. Evolving this model requires a rule of transferring the load between elements, following the breaking of one such element. Given that the width of the distribution function from which the strength of the elements are drawn is finite, the universal macroscopic responses are determined by the range of this load redistribution [16]. The local (nearest neighbours, introduced in [17]) and mean-field (global load sharing [16]) limits are well studied but are rather idealized in view of the fact that any realistic stress concentration range in a solid is neither of these two extremes. Several attempts have been made to interpolate between these two limits [18, 19, 20, 21]. However, in the case of catastrophic failures, the stress at which the system just breaks (critical stress) becomes non-zero only when the range of interaction is sufficiently large, so that it suppresses any spatial stress concentration [21]. Hence, statistics that are qualitatively similar to experiments [22] are observed only in the mean-field limit.

The above case of a fiber bundle model with system-wide loading can be contrasted with the case of a model where a load can be applied locally [23], for example along one edge of a two-dimensional system of fibers. Some of the fibers along that edge will break, and will then transfer their load to the surviving neighbours, on both sides of the broken fiber, within some range along that edge (see Sec. 2 and Fig. 1). The stress concentration and dynamics of this model is, therefore, constrained to an ‘activity front’, on one side of which all fibers are broken and the other side of which is completely intact. Such confinement of activity can also be achieved with system-wide loading, and a gradient in the failure thresholds of the fibers [20] in the direction perpendicular to the desired front.

The activity front, or the failure interface, can be driven through the system quasi-statically, giving rise to intermittent dynamics. The phase transition associated with these intermittent dynamics is the depinning transition of the interface (see e.g. [11, 24]). The states to either side of this critical point lie in the depinned phase, where the interface moves with a finite steady state velocity, and the pinned phase, where the interface is stopped by pinning centers (see e.g. [12]). This situation is widely observed in different physical systems, for example the vortex lines in superconductors [25], domain walls in magnetic systems [24], charge density waves [26], contact line dynamics in wetting [27] and, of course, in mode-I crack opening [28], on which we shall focus.

Unlike the case of catastrophic failure, in the interface depinning model even the extreme case of a nearest neighbor interaction will have a finite critical load at which the interface depins. It therefore gives a chance to study the effect of spatial fluctuations on interface dynamics. Previous studies regarding interface propagation in fiber bundles include simulations where the fibers were fixed between a rigid ceiling and a soft bottom plate [29]. For a single point loading and redistribution along the interface, the damaged region grew radially outwards on average, resulting in a continuously growing interface [23]. The interface length was proportional to the applied load, resulting in a steady value of the load per fiber along the interface. The intermittent dynamics of the interface showed scale-free statistics.

In our work, a systematic study of the roughness and avalanche dynamics of the fiber bundle model is made by varying the range of interaction along a propagating interface. In particular, we first consider a finite interaction range that can vary from the nearest neighbours to the entire breadth or width of the interface (mean field). This can include many different types of interaction that have a finite interaction range, for example those due to geometric effects like confinement to a thin sheet, plastic deformation, finite agglomerate size, etc. In such systems we demonstrate a crossover value of the range of interaction of the load redistribution that separates the local and mean-field behaviors. Secondly, we consider a scale-free interaction, where the load from a broken fiber is shared amongst all the fibers along the interface, in an amount inversely proportional to the distance of the fibers from the broken one, raised to some power. Among the scale-free interaction ranges, the inverse-square interaction has been considered before [30], inspired by the stress concentration field around a crack in an infinite sample. The inverse square interaction, however, is not guaranteed for a finite sample [31, 32], which is often a realistic scenario. For example in the fracture or debonding of a paint film, or other thin coating, the stress is redistributed over a distance comparable to the film thickness [33]. Also the range of the interaction in a real material sample can be affected by the correlation length of any disorder (see e.g. [34]) or the size of a plastic or process zone in a ductile metal [35, 36], for example. We find that the inverse square interaction lies in the middle of a continuously changing set of critical exponents for the roughness and avalanche size distributions. The model starts deviating from mean-field behavior as soon as the average range of the interaction is finite.

In the following, we first describe our model and then present the numerical results obtained from it. We give analytical calculations for the nearest-neighbor interaction and show that this case is qualitatively different from an elastic interface model approach in that limit. Finally we make comparison with mode-I crack propagation experiments and offer some conclusions about the effect of finite range interactions on fracture problems.

2. Model

We model the crack front of a mode-I fracture by a line of breakable fibers, as sketched in Fig. 1. Essentially, we store the stress profile and the position of the front in a

one-dimensional array, which is periodically updated. When the stress on an element exceeds its failure threshold, drawn randomly from a uniform distribution in $[0 : 1]$, there is a local failure and the front at that point is advanced by an amount proportional to the stress at that point prior to the failure. Hence, while the locations of the fibers are regular and discrete along the front, they are continuous along the propagation direction. After a fiber is advanced, the stress on it is set to zero. The stress that it had carried is partly dissipated (a fraction δ) and the rest (the fraction $1 - \delta$) is redistributed along the rest of the fracture front, as detailed below. In this way the one-dimensional front propagates along a two-dimensional fracture plane.

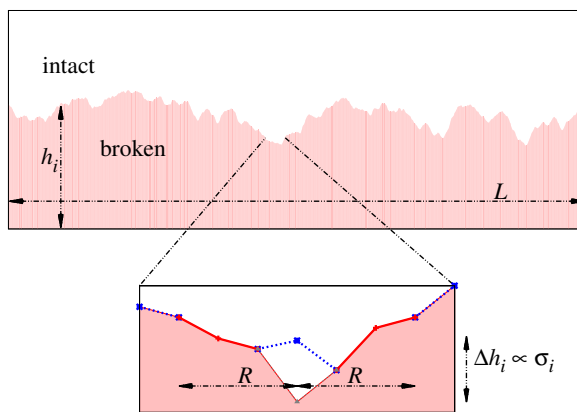


Figure 1. A snapshot of the interface between the broken (red) and unbroken (white) parts of the model system is shown. A magnified portion of the interface demonstrates the breaking of an element along the fracture front (dotted line) and the subsequent advancement of the front. The load of the broken fiber is redistributed to $R = 3$ neighbours (shown in red).

By construction the fracture front can only move forward, hence no islands or overhangs are allowed along the front. The total displacement of the i -th element, $h_i(t)$, upto time t is proportional to $\sum_{t \in \mathcal{T}_f} \sigma_i(t)$, where $\sigma_i(t)$ is the instantaneous stress at position i and \mathcal{T}_f is the set of all the times where a fiber failed at that location. Note that the proportionality constant has no effect on the macroscopic measures studied here. The dynamics of the front, except for the stress redistribution rule, are those followed in Ref. [30].

We will deal with two types of redistribution rules, following the breaking of a fiber. First, we will consider the case where the redistribution only affects fibers within a finite range, which can be as small so as to include only the nearest neighbours, or as large as the system size. For this we consider the uniform redistribution of the load (stress) to R neighbours on each side of the failed fiber (i.e. affecting a total of $2R$ fibers). Redistributions that affect a finite range are expected to be captured by this process, which is also the case for the catastrophic failure [21]. The two extremes are nearest neighbor ($R = 1$) and mean-field ($R \sim L$, where L is the system size) interactions and

we find a crossover length scale R_c above which the system starts behaving like the mean-field limit.

Secondly, we will consider scale-free redistribution, i.e. if the fiber at the i -th site fails then a fiber at the j -th site will receive a load proportional to $1/|i - j|^\gamma$. Here, for small enough values of γ , and hence more long-range coupling, the interaction is expected to be mean-field. For sharp enough decay (large γ values) the behavior will be local. Once again, a crossover $\gamma_c = 1$ is found above which the behaviour of the activity front starts deviating from mean-field limit. The system also then shows a continuous variation in its critical exponent values for roughness and avalanche size, until it reaches the other limit, a nearest neighbor interaction, for large enough γ .

3. Results

3.1. Load sharing over a finite range

The fracture front propagating through the system shows a depinning transition [40] when sufficient load is applied. This depinning transition is seen in the limit of no dissipation i.e. $\delta = 0$, or, in practice, negligibly small as compared to the total load ($\delta \ll 1$). It is an active-absorbing kind of phase transition [37]. The order parameter is defined here as the rate of activity, or the number of fibers breaking per Monte Carlo time-step. For a large enough load it reaches a stationary non-zero value (active state). When the load per fiber is below some critical value σ_c , it falls to zero (absorbing state). Fig. 2(a) shows the phase boundary between these active and absorbing states for different R values. The colour (shade) gradient gives the activity rate A . The $R = 1$ case shows a sharp jump (see Fig. 2(b)), suggesting a discontinuous transition there.

First we briefly look into the critical behavior for the nearest neighbor ($R = 1$) case without dissipation. Consider the situation where a load σ , per fiber, is applied uniformly and suddenly on the system. All fibers with a failure threshold below σ will break. This will create broken patches, the largest of which is most likely to contribute to further breaking the system, leading to depinning. If all the stress from this patch, of length l , is redistributed to the two neighboring points on either side of the patch, these points will now each carry load $\sigma + \frac{\sigma l}{2}$. Since l is large, this will likely cause further breaking and in the next time step the increased stress at the edge of the growing active region will be $\sigma + \frac{1}{2} \left(\sigma + \frac{l\sigma}{2} \right)$. After m such steps, the load on the sides of the patch will be

$$\begin{aligned} \sigma_E &= \left(\sigma + \frac{\sigma}{2} + \frac{\sigma}{4} + \dots + \frac{\sigma}{2^m} \right) + \frac{l\sigma}{2^m} \\ &= 2\sigma + \frac{\sigma(l-1)}{2^m}. \end{aligned} \tag{1}$$

The second term is an exponential decay, which vanishes for large m . The first term will cause depinning i.e. breaking all possible pinning centers, only when the stress exceeds the maximum pinning threshold 1, giving a critical load $\sigma_c = 1/2$. The above calculation is valid in the sub-critical limit, where large m values are possible, therefore

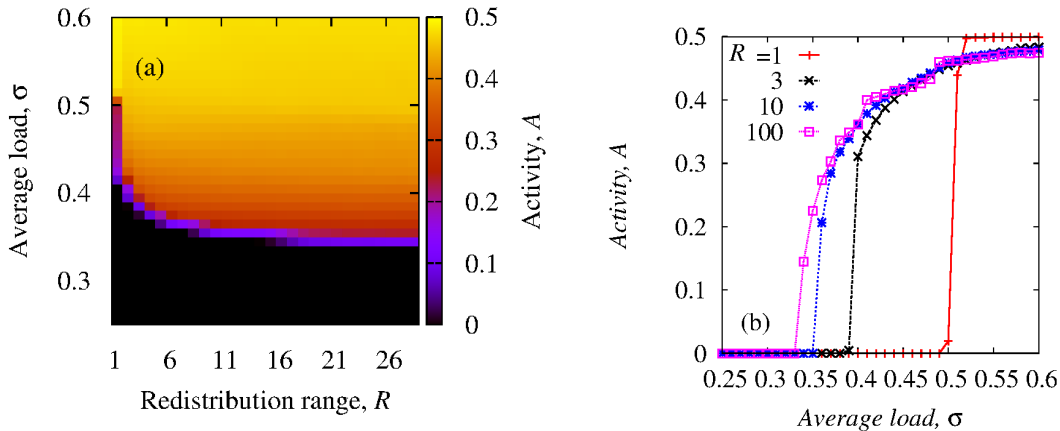


Figure 2. (a) The phase diagram for the depinning transition with a range dependent load transfer. The colour scale gives the steady-state breaking rate or activity, A for simulations run at different loads σ and ranges R . As can be seen, the nearest neighbor case $R = 1$ shows a sharp jump in the activity at the critical point $\sigma = 0.5$. In the presence of dissipation ($\delta > 0$), and for a slow quasi-static drive, the critical point becomes an attractive fixed point, causing the load per fiber to saturate at its critical value. (b) Activity rates for various values of R show how its discontinuous jump for $R = 1$ gradually disappears as R becomes large. The system size is $L = 1000$.

giving the limiting stress that the system can withstand without depinning. This is the critical load that we see in the simulations as well (see e.g. Fig. 2 for $R = 1$). Also, at the critical load $1/2$, it is trivially seen that half of the system on average will break in the first time step following the loading. After redistribution of this load, the surviving fibers will have stress 1 on average and will then break in the following time step. These two steps will continue to repeat in the steady state, giving an average activity rate of $1/2$. Note that this is a discontinuous jump from zero activity in the absorbing phase (for $\sigma < \sigma_c$). This is in contrast to nearest neighbor elastic line (Edwards-Wilkinson model [38]) depinning, which shows a continuous transition [39] instead.

The other extreme case is the continuous depinning transition in the mean-field limit ($R \sim L$). Unsurprisingly, the mean-field exponents are recovered there (see Appendix A).

For quasi-static loading, the external force increases slowly with time, like the case of peeling a piece of tape off a table. This increase in load can cause fibers to break, and thereby advance the fracture front. However, in any real experiment there must be a finite dissipation of stress as the front advances. This can be due to acoustic emissions, friction, heat, etc or simply the finite compliance of any load cell. The dissipation will halt any advance, but the increase in load will then continue until another advance happens, and so on. These two competing mechanisms, loading and dissipation, lead to intermittent dynamics of the front. In our simulations we capture this by alternating between slow loading and fast front activity, including dissipation. Now the load is increased until the first fiber breaks, then it is stopped and the load redistribution

rules are followed until the avalanche of activity stops, on the assumption that internal load redistribution occurs much faster than the recovery of the external loading. When dissipation stops the avalanche, further loading is continued. In this way any system will self-organize, tending towards the critical point of the depinning transition in the corresponding conservative system (Fig. 2). In the following we will study the dynamic (avalanche statistics) and static (roughness of the front) properties of the dissipative system for different load redistribution rules, including the local and mean-field limits, and intermediate conditions. We aim to understand the crossover dynamics between the two very different end-members of this model, and to determine the redistribution range at which the model behavior shifts from local to mean-field.

3.1.1. Intermittent dynamics: Avalanche statistics Let us now explore the critical response to quasi-static loading in the presence of dissipation. After an initial failure the load is redistributed, as described above, and a fraction of the load from each failing fiber is dissipated. The dissipation implies that the front propagation will eventually halt, at which point we resume increasing the load, slowly, to restart the dynamics. The total number of fibers breaking between two successive loading steps, denoted by S , measures the size of an avalanche. The number of load redistribution steps before the avalanche stops is the duration of the avalanche T . In Fig. 3 the size distribution, $P(S)$, and duration distribution, $Q(T)$, of the avalanches are plotted for different values of R . Both distributions show a crossover in the exponent value of a power-law fit, beyond a given size (or duration), and the crossover size (duration) increases with increasing R . While a precise crossover scale will be obtained later (Sec. II.3), from these plots it is intuitively clear that for a given R small avalanches will not see the scale of load redistribution and will give mean-field statistics, since the load distribution within that range is uniform. Only the larger avalanches, involving several redistribution steps, will feel the effect of the load redistribution range and hence deviate from mean-field behavior.

3.1.2. Roughness exponent of the front The response of the system in the vicinity of the depinning critical point can be studied from its dynamics, as done above, and also from its static characteristics, for example in the roughness of the propagating front. The self-similar nature of the front, at any given moment, in the case of fracture is well studied (see Ref. [40] for a review). In order to demonstrate the roughness properties of our model, we measure the amplitude of the height fluctuations

$$C(r) = \langle (h_{i+r} - h_i)^2 \rangle^{1/2} \sim r^\zeta, \quad (2)$$

where the angular bracket is the average over space and ζ is the roughness or Hurst exponent. Figure 4(a) depicts the behavior of the roughness as the interaction range R is varied. As in the case of avalanche statistics, the scaling functions also show a crossover in critical exponent, depending on the value of R . Clearly, as long as $r < R$, $C(r)$ should be independent of r , since there is no notion of spatial distance within that

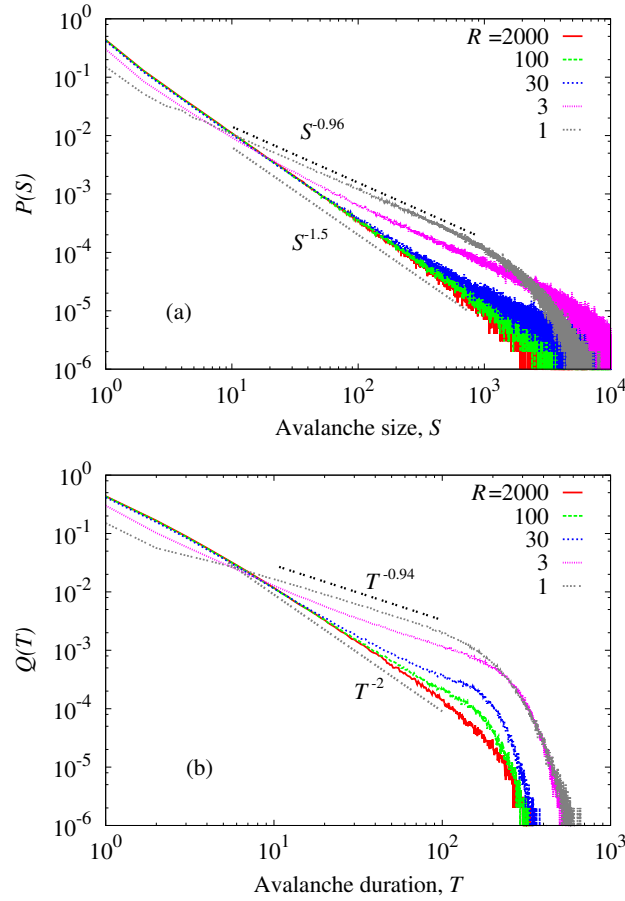


Figure 3. The size (a) and duration (b) distributions of avalanches are shown for different values of R and a system size $L = 10000$. A crossover in the exponent values for size (duration) is seen from a mean-field value of 1.5 (2) to a local value of 0.96 (0.94). The latter scaling exponents are best-fit values to the numerical results at $R = 1$. As discussed in the text, smaller avalanches do not see the load sharing range R , hence follow mean-field statistics.

range. In other words, for $r < R$ the system should be mean-field-like. It is only when correlation is sought over a length-scale larger than R that a non-trivial variation in $C(r)$ is observed, with $\zeta \approx 0.9$. This point is further clarified in Fig. 4(b), where the distance r is normalized by R . All curves then show the same crossover in roughness near the point $r \approx R$.

3.1.3. Crossover scale For a more precise measure of the crossover scale, we look at the long time average of the load per fiber (which is also the critical stress σ_c) on the system for different values of R . In the mean-field limit, the stress is expected to saturate to $1/3$, as was the case in Ref. [23]. We therefore look at the quantity $\Delta\sigma_c = \sigma_c(R, L) - 1/3$, which will tend to zero as either R and L is increased. For a given system size, however, finite size effects will make it saturate at a small but finite value. A crossover scale, consistent with our usage in previous sections, can be defined from the point where

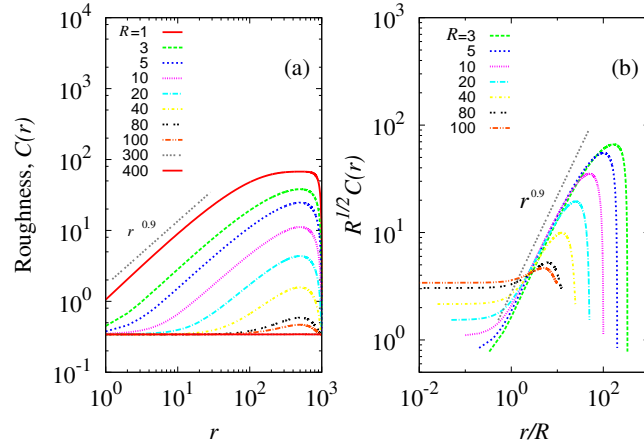


Figure 4. (a) The self-similar scaling of the roughness of the front is shown, following the measure given in Eq. (2). The height fluctuations in the mean-field limit ($r/R \rightarrow 0$) show no variation with r , since there is no notion of distance below the length scale R . (b) When distance is scaled by R , all crossover points collapse to the same value, as does the scaling of the roughness both above and below the point $r = R$. The system size is $L = 1000$.

$\Delta\sigma_c$ starts becoming independent of R . Quantities behaving independently of R are the signature of the mean-field limit.

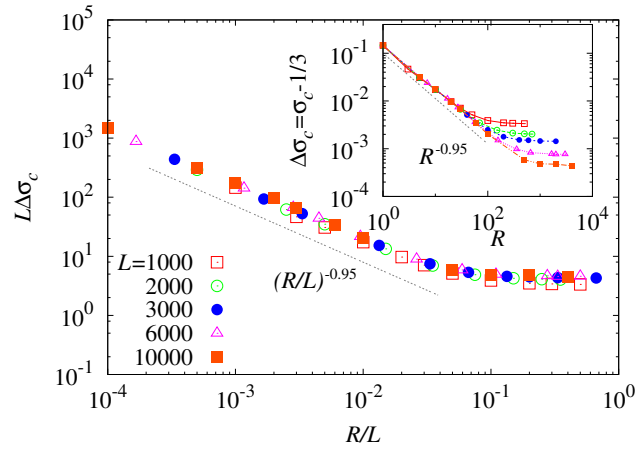


Figure 5. The inset shows how the critical load approaches the mean-field limit as R increases. Beyond some crossover value R_c , the quantity $\Delta\sigma_c$ becomes independent of R , signaling the change from local to mean-field behavior. The main panel shows how all data collapses when scaled by system size, confirming that $R_c \sim L$. In other words, when R is larger than roughly 10% of the system size, the system behaves like the mean-field case.

In Fig. 5 the dependence of $\Delta\sigma_c$ on the redistribution range R for different system sizes is plotted. The inset shows how the crossover behavior depends on the system size, and also demonstrates how $\Delta\sigma_c$ decreases to zero as the system size grows. Data collapse is obtained by scaling the distance with L . This implies that $R_c \sim L$, or that

a significant fraction of the system must be covered by the load sharing range in order for the system to show mean-field like behavior.

3.2. Scale-free load sharing

Finally, we study the effect of varying the load redistribution process. Now, following a failure at site i , the load received at site j will be proportional to $\rho = \frac{1}{|i-j|^\gamma}$. As one example of such a response, linear-elastic theory predicts an inverse square ($\gamma = 2$) [41, 42] load redistribution for an infinite sample. However, the redistribution range and scaling behavior can be modified due to effects such as a finite sample [31, 32], the width of the sample [33], any correlation in the local disorder [34], and so on. In such situations, a scale free load redistribution is closer to what one can expect, instead of the finite range interaction presented in the preceding sections.

The case $\gamma = 2$, which corresponds to a classic Inglis crack, was studied in Ref. [30]. But here we show that the $\gamma = 2$ case lies in the middle of a continuously varying ‘universality’ that interpolates between local and global scenarios. Hence a small change in γ can lead to a significant change in macroscopic observables, such as activity statistics and roughness exponents.

Before summarizing the numerical results, let us briefly look into how the crossover value of the exponent γ may be predicted from the linear scaling of R_c with system size obtained in the previous section. Even for a ‘scale-free’ distribution there are still two obvious scales: the lower cut-off scale of the interaction range is the lattice spacing and upper cut-off is the system size. Hence its possible to define an effective range $R_{eff} = \int_1^L r \rho(r) dr$ with $\rho(r)$ being the (normalized) power-law redistribution of load. It can be shown [21] that $R_{eff} = \frac{1-\gamma}{2-\gamma} \frac{L^{2-\gamma}-1}{L^{1-\gamma}-1}$. For $1 < \gamma < 2$, $R_{eff} \sim L^{2-\gamma}$, which must match with $R_c \sim L$ at the crossover point. This gives $2 - \gamma_c = 1$ i.e. $\gamma_c = 1$. So for any value of γ larger than 1, the average redistribution range of the load will be smaller than the system size, and thus mean-field-like behavior can no longer be expected. However, as we shall see, this deviation from the mean-field response does not necessarily imply local load sharing behavior for other measures, such as the avalanche and roughness statistics.

Note that $\gamma_c = 1$ is also an intuitive result from the fact that for $\gamma \leq 1$ the effective range diverges for an infinite system. But that does not exclude the possibility of a mean-field response where $\gamma_c > 1$, which is indeed the case for catastrophic breakdown [21]. Therefore, the above result is a joint consequence of the linear scaling $R_c \sim L$ and the divergence of the effective range for $\gamma \leq 1$.

In Fig. 6(a), the avalanche size distributions are plotted for different γ values. They show a continuous variation in the exponent τ of the size distribution, $P(S) \sim S^{-\tau}$, as detailed in Fig. 7 (b). As expected, the departure from the mean-field value ($\tau = 1.5$) starts from just above $\gamma_c = 1$. Figure 7 (a) further shows the scaling of the roughness for different γ values. A power-law fit following Eq. (2) is used to find the value of the exponent ζ for each γ , and these roughness exponents are shown in Fig. 7(b). For the

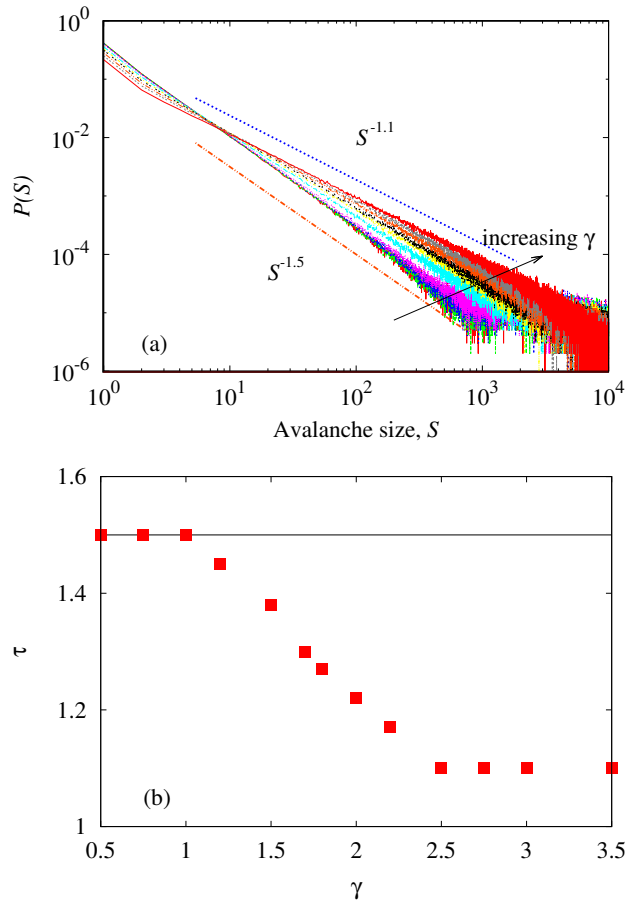


Figure 6. (a) The avalanche size distributions $P(S)$ are plotted for different values of γ . They have the scale invariant form $P(S) \sim S^{-\tau}$. The exponent τ varies with γ as shown in panel (b). As mentioned in the text, the departure from the mean-field exponent 1.5 is seen for $\gamma > \gamma_c = 1$. The system size is $L = 10000$.

similar situation of a fluctuating elastic line, both theory [43] and simulations [44] predict a relation $\zeta = (2\gamma - 3)/3$, which is also plotted in the graph. While near $\gamma = 2$ it follows our simulation points well, away from this intermediate case deviation is significant. This further underlines the difference between the macroscopic modeling approach of the elastic line and the microscopic discrete model studied here. They differ qualitatively as the interaction range becomes localized, while keeping the correspondence near the linear-elastic regime at $\gamma = 2$.

4. Discussion and conclusion

The common features that arise in various physical systems such as domain walls in magnetic materials, vortex lines in superconductors, charge density waves, contact line dynamics in wetting and also in mode-I fracture front, is that an “elastic” line or front is driven by an external parameter (a magnetic field, mechanical force, etc.) through a medium with many obstacles (impurities, variations in breaking strength, etc.). This

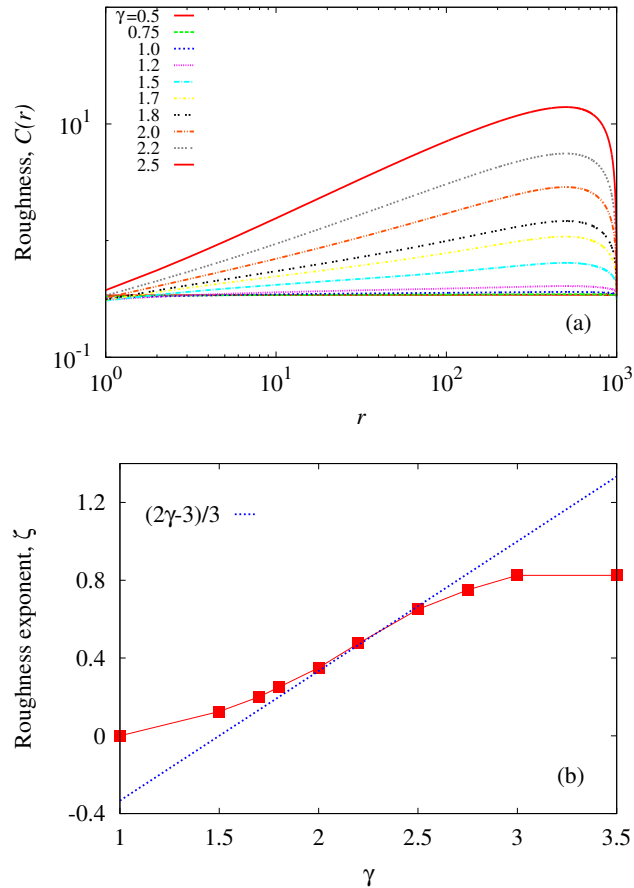


Figure 7. In panel (a), the scaling of the roughness of the front is shown for different values of γ . As in Fig. 4, in the mean-field limit $C(r)$ is independent of r and starts departing from this behavior when $\gamma > 1$. The continuous variation of the roughness exponent ζ with γ is shown in panel (b). Near $\gamma = 2$ it matches with the theoretical prediction [43, 44], shown by the dotted line, of a fluctuating elastic line near. The system size is $L = 1000$.

results in intermittent dynamics of the moving front. The classification of the properties of such a front depends on its elastic nature, or in other words, the range upto which the front is affected following a local perturbation.

Here we have reported the critical properties of such a front through a simple, discrete fiber bundle model approach. The different strengths of the fibers represent the disorder in the material. While this is a generic model for interface propagation in the cases mentioned above, we focused on mode-I fracture front propagation in this study. Assuming the applied load to be localized along one side, we can track the activity of the front through this model. We aimed at determining the influence of a variable range of interaction, characterizing the load redistribution range following the failure of a fiber along the interface, on macroscopic static and dynamic properties of the interface, such as roughness and avalanche statistics. We found such macroscopic observables to be very sensitive to the range of interaction. In particular, we could identify a crossover

from local, nearest-neighbor-like behavior to global, mean-field-like behavior by varying the range of load redistribution. We showed how this could be done directly, using a flat distribution over a finite neighborhood, or indirectly by varying the exponent γ in the case of a power-law load redistribution. The crossover range R_c scales linearly with the system size in the case of a finite range redistribution. This situation corresponds to $\gamma_c = 1$, for which the behavior deviates from the mean-field in the case of power-law load redistribution. For a power-law load redistribution, a continuously varying set of exponents are obtained for the avalanche size statistics and the roughness of the front. Interestingly, the $\gamma = 2$ case lies in the middle of such a continuous variation, implying that any change in γ will be reflected in the roughness and avalanche size exponent values.

An obvious point of comparison for these results is with the elastic interface model [45]. This model is formulated from an opposite approach to ours, in the sense that it is a macroscopic model. Models of this type consider the elastic interactions of the interface line from the perspective of linear-elastic fracture mechanics, where the disorder of the material is treated as quenched noise, as opposed to a microscopic modeling of the disordered solid. The elastic interaction can fall off with distance r from a local perturbation as $1/r^\gamma$. Similar characterization by varying the parameter γ leads to a continuous variation in the roughness exponent value [44], and also crossover behavior [46]. But apart from the mean-field limit, or dimensions higher than 4 [47], it is both quantitatively (see Fig. 7) and qualitatively different (e.g. for fiber bundle the depinning transition is discontinuous for the nearest neighbor interaction) from the fiber bundle model of an interface.

Many experiments have been done on fracture front propagation in disordered solids in the last couple of decades [5, 6]. Among other things, they concern themselves with in and out-of-plane roughness properties of the broken surfaces, measured both along and perpendicular to the direction of the crack front [40]. The situation is somewhat simplified when out of plane roughness is suppressed and the crack propagates along an easy plane only, resembling the in-plane motion of the front studied here. Particularly, in Ref. [11] two Plexiglas plates were sandblasted, joined together and then slowly forced open from one edge such that a mode-I crack opening took place. The propagating front was viewed by the loss of transparency of the joined plates. The avalanche dynamics and roughness properties of such fronts are well studied [48, 49, 12, 13]. Apart from showing a crossover in response from small-to-large length scales, the roughness exponent measurements also show differences in these two limiting regions. The avalanche exponent can be significantly lower (1.1) than predicted (1.28) by the elastic interface model with inverse square elastic strength [32], but also there exists a large spread in the measured values of such exponents in different experiments [22]. Such a spread is not unique to the case of fracture front propagation, but is also seen in the cases of domain wall dynamics in magnetic systems [50, 51, 52], and fluid invasion fronts in porous media [53]. Although several mechanisms were proposed to explain these differences, such as driving rate, correlation in disorder, microscale coalescence

and so on, no consensus has yet been reached. Our simulation shows how one can relate such a change in exponent values with the variation of an effective interaction range, which in turn can be due to one or more of the reasons mentioned above.

In conclusion, the interface propagation in the fiber bundle model shows a crossover behavior from local to mean-field statistics as the range of the interaction is increased. The crossover length scales linearly with the system size. This implies that for power-law load sharing for exponent values greater than one, the behavior will be different from the mean-field. This simple prediction is also confirmed numerically. A continuous variation in the avalanche size and roughness scaling exponent values were seen with different powers of the scale-free load sharing, making it a very relevant parameter to keep in mind while considering the finite scales of interaction that might arise in experimental situations.

Appendix A. Depinning transition exponents in the mean field limit

When $R \sim L$, the depinning transition seen in our model is the mean-field type. The growth of the order parameter, here the activity rate, above the critical load behaves as $A \sim (\sigma - \sigma_c)^\theta$. Assuming the scaling form

$$A(t) \sim t^{-\delta} F\left(t^{1/\nu} |\sigma - \sigma_c|, t^z/L\right), \quad (\text{A.1})$$

we can estimate the scaling exponents δ , ν and z and also verify the scaling relation $\delta = \theta/\nu$, in this limit.

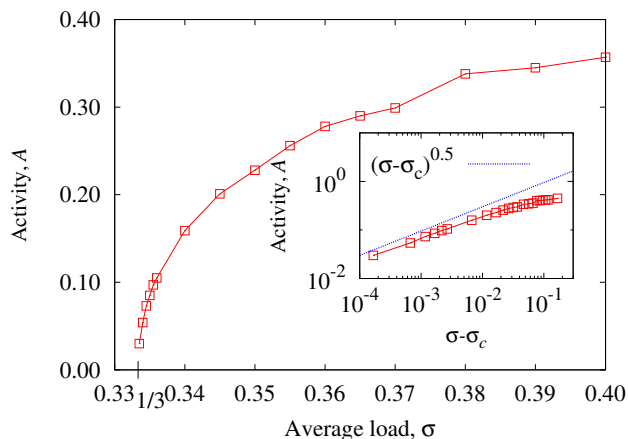


Figure A1. The growth of the order parameter A beyond the critical load σ_c is shown. The inset shows the power-law fitting with an order parameter exponent value $\theta = 1/2$. The system size is $L = 100\,000$.

In Fig. A1 we plot the saturation activity rates at different σ values above $\sigma_c = 1/3$ for the mean-field case of $R = L$. The inset shows the power-law variation $(\sigma - \sigma_c)^{1/2}$, giving $\theta = 1/2$, which matches with the prediction for the mean-field elastic interface [54]. At the critical point the order parameter decays as $A(t) \sim t^{-\delta}$, where t is the time measured by the number of load redistribution steps. This is seen in Fig. A2, with

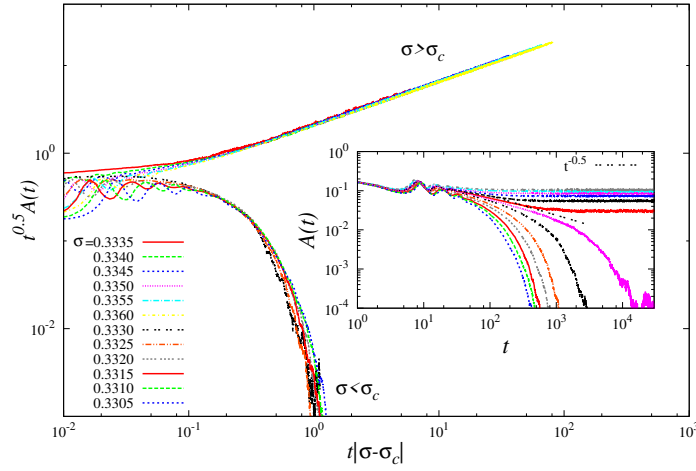


Figure A2. The super-critical and sub-critical behavior of the order parameter with time are shown. At the critical point a power-law decay gives the exponent $\delta \approx 0.5$ and the off-critical collapse shows gives the scaling exponent $\nu = 1.0$. The system size is $L = 100\,000$.

$\delta \approx 0.5$. Also, by plotting $A(t)t^\delta$ with $t|\sigma_c - \sigma|^\nu$ and by tuning ν , we get a data collapse near $\nu \approx 1.0$ (see Fig. A2). This agrees with the scaling relation $\delta = \beta/\nu$. Finally, for the finite size scaling at the critical point, the cut-off time scale τ scales with system size as $\tau \sim L^{1/z}$ with $z \approx 2.0$. This set of exponents defines the mean-field depinning transition for fiber bundle interfaces, and these results show that our model reaches this well-defined response in the appropriate limit.

References

- [1] F. T. Peirce, *J. Text. Inst.* **17**, T355 (1926).
- [2] H. E. Daniels, *Proc. Royal Soc. London A* **183**, 405 (1945).
- [3] S. L. Phoenix, H. M. Taylor, *Adv. Appl. Prob.* **5**, 200 (1973).
- [4] B. K. Chakrabarti and L. G. Benguigui, *Statistical Physics of Fracture and Breakdown in Disordered Systems* (Oxford University Press, Oxford, 1997).
- [5] M. Sahimi, *Heterogeneous Materials II: Nonlinear and Breakdown Properties* (Springer, New York, 2003).
- [6] S. Biswas, P. Ray, B. K. Chakrabarti, *Statistical physics of fracture, breakdown and earthquake* (Wiley, 2015).
- [7] A. Garcimartin, A. Guarino, L. Bellon, S. Ciliberto, *Phys. Rev. Lett.* **79**, 3202 (1997).
- [8] A. Guarino, A. Garcimartin, S. Ciliberto, *Eur. Phys. J. B* **6**, 13 (1998).
- [9] S. Deschanel, L. Vanel, G. Vigier, N. Godin, S. Ciliberto, *Int. J. Fract.* **1**, 87 (2006).
- [10] L. I. Salminen, A. I. Tolvanen, M. J. Alava, *Phys. Rev. Lett.* **89**, 185503 (2002).
- [11] J. Schmittbuhl, K. Måløy, *Phys. Rev. Lett.* **78**, 3888 (1997).
- [12] S. Santucci, M. Grob, R. Toussaint, J. Schmittbuhl, A. Hansen, K. J. Måløy, *EPL* **92**, 44001 (2010).
- [13] J. Chopin, A. Boudaoud, M. Adda-Bedia, *J. Mech. Phys. Solids* **74**, 38 (2015).
- [14] D. Amitrano, J. R. Grasso, G. Senfaute, *Geophys. Res. Lett.* **32**, L08314 (2005).
- [15] D. Cohen, P. Lehmann, D. Or, *Water Resource Res.* **45**, W10436 (2009).
- [16] S. Pradhan, A. Hansen, B. K. Chakrabarti, *Rev. Mod. Phys* **82**, 499 (2010).

- [17] D. G. Harlow, S. L. Phoenix, J. Compos. Mater. **12**, 195 (1978).
- [18] R. C. Hidalgo, Y. Moreno, F. Kun, H. J. Herrmann, Phys. Rev. E **65**, 046148 (2002).
- [19] S. Pradhan, B. K. Chakrabarti, A. Hansen, Phys. Rev. E **71**, 036149 (2005).
- [20] A. Stormo, K. S. Gjerden, A. Hansen, Phys. Rev. E **86**, 025101(R) (2012).
- [21] S. Biswas, S. Roy, P. Ray, Phys. Rev. E **91**, 050105(R) (2015).
- [22] D. Bonamy, J. Appl. Phys. D **42**, 214014 (2009).
- [23] S. Biswas, B. K. Chakrabarti, Phys. Rev. E **88**, 042112 (2013).
- [24] S. Zapperi, P. Cizeau, G. Durin, H. E. Stanley, Phys. Rev. B **58**, 6353 (1998).
- [25] A. I. Larkin, Yu. N. Ovchinnikov, J. Low Temp. Phys. **34**, 409 (1979).
- [26] D. S. Fisher, Phys. Rev B **31**, 1396 (1985).
- [27] T. Chevalier, L. Talon, Eur. Phys. J. B **38**, 76 (2015).
- [28] J. P. Bouchaud, E. Bouchaud, G. Lapasset, J. Planes, Phys. Rev. Lett. **71**, 2240 (1993).
- [29] G. G. Batrouni, A. Hansen, J. Schmittbuhl, Phys. Rev. E **65**, 036126 (2002).
- [30] G. Pontuale, F. Colaioni, A. Petri, EPL **101**, 16005 (2013).
- [31] J. W. Hutchinson, Z. Suo, Adv. Appl. Mech. **29**, 63 (1991).
- [32] J. Barés, M. L. Hattali, D. Dalmas, D. Bonamy, Phys. Rev. Lett. **113**, 264301 (2014).
- [33] Z. C. Xia, J. W. Hutchinson, J. Mech. Phys. Solids **48**, 1107 (2000).
- [34] C. Peng, S. Havlin, M. Schwartz, H. E. Stanley, Phys. Rev. Lett. **44**, R2239 (1991).
- [35] G. I. Barenblatt, J. Appl. Mech. Solids **23**, 434 (1959).
- [36] D. S. Dugdale, J. Mech. Phys. Solids **8**, 100 (1960).
- [37] *Non-equilibrium phase transitions*, M. Henkel, H. Hinrichsen, S. Lübek, Springer (2014).
- [38] S. Edwards, D. Wilkinson, Proc. R. Soc. A **381**, 17 (1982).
- [39] L. Amaral, A. Barabási, H. Makse, H. E. Stanley, Phys. Rev. E **52**, 4087 (1995).
- [40] D. Bonamy, E. Bouchaud, Phys. Rep. **498**, 1 (2011).
- [41] J. Schmittbuhl, S. Roux, J-P. Vilotte, K. J. Måløy, Phys. Rev. Lett **74**, 1787 (1995).
- [42] S. Ramanathan, D. Ertas, D. S. Fisher, Phys. Rev. Lett. **79**, 873 (1997).
- [43] O. Narayan, D. S. Fisher, Phys. Rev. B **48**, 7030 (1993).
- [44] A. Tanguy, M. Gouelle, S. Roux, Phys. Rev. E **58**, 1577 (1998).
- [45] J. R. Rice, J. Appl. Mech. **52**, 571 (1985).
- [46] Y. J. Chen, S. Zapperi, J. P. Sethna, Phys. Rev. E **92**, 022146 (2015).
- [47] P. Le Doussal, K. J. Wiese, Phys. Rev. E **79**, 051106 (2009).
- [48] K. Måløy, J. Schmittbuhl, Phys. Rev. Lett. **87**, 105502 (2001).
- [49] K. Måløy, S. Santucci, J. Schmittbuhl, R. Toussaint, Phys. Rev. Lett. **96**, 045501 (2006).
- [50] S. Zapperi, P. Cizeau, G. Durin, H. E. Stanley, Phys. Rev. B **58**, 6353 (1998).
- [51] B. Alessandro, C. Beatrice, G. Bertotto, A. Montorsi, J. Appl. Phys. **68**, 2901 (1990); **68**, 2908 (1990)
- [52] D. Kim, S. Choe, S. Shin, Phys. Rev. Lett. **90**, 087203 (2003).
- [53] S. He, G. Kahanda, P. Wong, Phys. Rev. Lett. **69**, 3731 (1992).
- [54] J. Vannimenus, B. Derrida, J. Stat. Phys. **105**, 1 (2001).